Journal of Sound and Vibration 329 (2010) 1254–1273

Contents lists available at ScienceDirect

Journal of Sound and Vibration

journal homepage: www.elsevier.com/locate/jsvi

A tunable high-static–low-dynamic stiffness vibration isolator

N. Zhou, K. Liu *

Department of Mechanical Engineering, Lakehead University, Thunder Bay, Canada P7B 5E1

ARTICLE INFO

Article history:
Received 15 July 2009
Received in revised form
28 October 2009
Accepted 2 November 2009
Handling Editor: A.V. Metrikine
Available online 3 December 2009

ABSTRACT

In this study, a novel vibration isolator is developed. The developed isolator possesses the characteristics of high-static–low-dynamic stiffness (HSLDS) and can act passively or semi-actively. The HSLDS property of the isolator is obtained by connecting a mechanical spring, in parallel with a magnetic spring that is constructed by a pair of electromagnets and a permanent magnet. The mechanical spring is a structural beam whose stiffness exhibits a hardening behavior. The stiffness of the magnetic spring can be positive or negative, depending on the polarity of the current to the electromagnets. A passive HSLDS isolator is obtained when the electromagnet current is zero. In the stiffness characterization study, the analytical model for each of the springs is established and the tuning parameters are identified. Using the stiffness models, the design optimization issues are investigated. In the experimental study, the effectiveness of the isolator for vibration isolation is tested. The analytical natural frequencies of the isolator are validated experimentally. The relationships between the displacement transmissibility and the exciting frequency are measured both under the passive mode and under the semi-active mode. The on-line tuning capability of the isolator is investigated.

1. Introduction

Excessive vibration can cause serious damage to structures and machines. Vibration isolation is an effective way to reduce vibration [1]. The methods of vibration isolation can be classified as: passive, active, and semi-active. A simple passive vibration isolator consists of a spring and damper. The design of the isolator spring and the isolator damper requires a trade-off. The dynamic stiffness of an isolator spring should be as low as possible in order to increase the region of vibration isolation. However, if a linear spring is used, low stiffness isolator causes unacceptably large static deflection. A desirable vibration isolator should possess high-static–low-dynamic stiffness (HSLDS) so that it can support a large load statically while having low dynamic stiffness. A HSLDS spring is a nonlinear spring. When an isolator has zero or near zero dynamic stiffness, it is referred to as a quasi-zero-stiffness (QZS) isolator.

There are a number of ways to obtain the HSLDS property. A detailed review of recent advances in nonlinear passive vibration isolators can be found in [2]. A common method to design a passive HSLDS isolator is to combine a positive stiffness spring with a negative stiffness spring. For example, in [3,4], a QZS isolator was obtained by connecting a vertical coil spring and two oblique coil springs. The oblique springs provide negative stiffness in the vertical direction which counteracts the positive stiffness of the vertical spring. Another way is to utilize structural buckling phenomena. In [5], the beam subject to an axial load was combined with a positive stiffness spring to achieve a QZS isolator. Axially loaded rods

* Corresponding author. Tel.: +1 807 343 8634; fax: +1 807 346 7943.
E-mail address: kliu@lakeheadu.ca (K. Liu).

0022-460X/$ - see front matter © 2009 Elsevier Ltd. All rights reserved.
doi:10.1016/j.jsv.2009.11.001

were used in [6] to improve vehicle driver vibration isolation. The studies conducted in [7,8] showed that a highly deformed pinched loop possesses a softening stiffness. It is well known that two permanent magnets can form a positive or negative stiffness spring, depending on their polarity arrangement. The HSLDS isolator proposed in [9] was made of two linear coil springs and three permanent magnets arranged in an attracting configuration.

In general passive isolators are incapable of coping with varying conditions such as changes in the exciting frequency or in system parameters. Active vibration isolators can achieve superior performance through a feedback system. However, they are not cost-effective. Semi-active vibration isolators, in which the system properties can be adjusted in real time, combine the advantages of both passive and active isolators. Semi-active vibration isolators preserve the reliability of passive isolators even in the event of power loss; they also possess the versatility and adaptability of active isolators. In a semi-active isolator, the isolation is achieved by passive elements whose properties can be changed on-line to maintain an optimal performance [10,11]. One common way to adjust the isolator's properties is to change its damping value. The damping value can be changed using a variable-orifice valve to alter the resistance to the flow of a hydraulic damper [12]. Most noticeably, electro-rheological or magneto-rheological dampers feature a broad bandwidth modulation of the damping characteristics through variations in the electrical or magnetic field [13–17]. Stiffness is another property that can be designed to be adjustable on-line. Several ways of obtaining variable stiffness devices are discussed in [18]. The tunable vibration isolator proposed in [19] achieves the stiffness variation through a separation of a compound leaf spring by a wax actuator.

Compared to mechanical or hydraulic devices, electromagnetic devices possess some unique advantages, such as cleanliness, faster response, no mechanical contact, easy integration with control system, and compactness. Therefore, the use of electromagnetic techniques in semi-active vibration control continues to receive considerable attention [20–26]. In the past, we have developed several electromagnetic apparatuses for vibration suppression. In [27], a damper based on the eddy-current principle was used to construct a tunable vibration absorber. In [28], a tunable electromagnetic vibration absorber was proposed. In [29], an active electromagnetic actuator was utilized to implement time-delay control.

In this study, we propose a tunable electromagnetic vibration isolator. The isolator comprises a mechanical spring and a magnetic spring. The developed isolator possesses HSLDS characteristics. This paper differs from the previous studies in three aspects. First, the mechanical spring used is a structural beam. In practice, structural members are frequently used as springs. However, most structural members exhibit a hardening effect which makes it more difficult to achieve the HSLDS property. Second, in contrast to the apparatus proposed in [9], the passive negative stiffness spring is obtained through interaction between the permanent magnet and the steel cores of the electromagnets. Third, the isolator can act either passively or semi-actively. Under the semi-active mode, the isolator's stiffness can be instantly decreased or increased without any moving parts.

The aim of the paper is twofold: to develop the analytical models for the proposed isolator and study the design optimization issues, and to test the performance of the isolator and demonstrate the effectiveness of the on-line tuning feature. The rest of the paper is organized as follows: In Section 2, the proposed tunable electromagnetic isolator is introduced. In Section 3, the stiffness characterization and optimum design issues are addressed. In Section 4, the experimental results are presented. In Section 5, the study conclusions are drawn.

2. Electromagnetic vibration isolator

Fig. 1 shows a schematic of the proposed electromagnetic vibration isolator. A steel beam (1) is used to support a permanent magnet (PM) (2). The permanent magnet acts as an isolated mass and is referred to as mass denoted as m. The mass-beam assembly is placed between a pair of electromagnets (EMs) (3). The tension of the beam can be adjusted by the screws (4). Each EM is constructed by winding Gauge 22 copper wire around a low-carbon steel bolt with a diameter of 13.0 mm. The outer diameter and length of the coil are 46.6 and 88.0 mm, respectively. The number of the turns is about 3565. As shown in Fig. 2, two springs are involved in the isolator. The beam acts a mechanical spring denoted as k_b. The interaction between the mass and the EMs results in a magnetic spring denoted as k_{pe}. The electromagnetic spring k_{pe} consists of two parts: k_{pc} and k_{pf} where k_{pc} is due to the interaction between the mass and the EM cores and k_{pf} the interaction between the mass and the flux generated by the EMs. It should be noted that the static stiffness depends only on the mechanical spring, while the dynamic stiffness comes from the combined effect of the mechanical spring and the electromagnetic spring. In order to assess the isolator performance and optimize its design, an analytical model for each of the aforementioned springs is needed. In what follows, first the analytical model for each of the springs is established. Then the analytical models for the combined systems are obtained and the optimization issue is discussed.

3. Stiffness characterization and design optimization

3.1. The mechanical springs

An analytical model for the stiffness of the beam is not readily available because the beam is subjected to an initial tension and has a large deformation. Thus the stiffness of the mechanical spring was determined experimentally. With the beam firmly clamped in place, a force was applied to the mass. The displacement of the mass was measured by a dial gauge

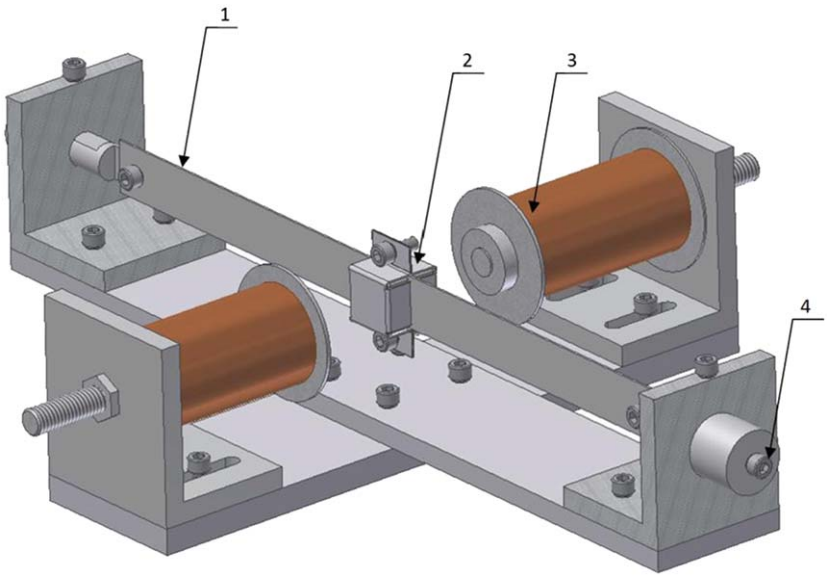

Fig. 1. Schematic of the tunable HSLDS isolator.

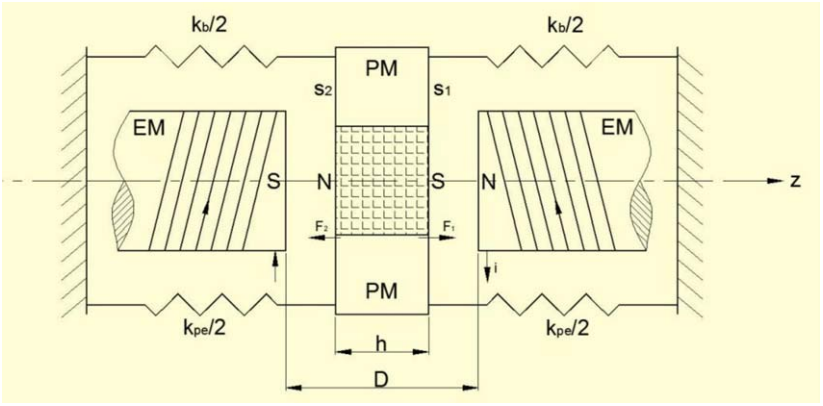

Fig. 2. Two springs involved in the tunable isolator.

and the corresponding force was measured by a force gauge. For each of the applied forces, the experiments were repeated five times to ensure the result consistency. Two types of beams were considered. The first one was a steel ruler with length × width × thickness of 32.0 × 15.0 × 0.5 mm. The second one was a steel saw blade with length × width × thickness of 28.0 × 12.0 × 0.6 mm. The tension applied to the second beam was higher than that applied to the first beam. Fig. 3 shows the averaged experimental results of the restoring force vs. the mass displacement. In the figure, circles represent the measured values for the first beam and boxes represent the measured values for the second beam.

A third-order polynomial is used to fit the data by the least-squares method. The best-fit force–displacement relationship for the first beam is given by

$$F_b = 1.0460 \times 10^3 z + 3.1861 \times 10^7 z^3, \tag{1}$$

where z denotes the displacement of the mass. The solid line in Fig. 3 represents the best-fit curve. The best-fit force–displacement relationship for the second beam is given by

$$F_b = 1.0503 \times 10^3 z + 3.1538 \times 10^6 z^3. \tag{2}$$

The dotted line in Fig. 3 represents the best-fit curve. Differentiating Eq. (1) yields the stiffness for the first beam

$$k_b = 1.0460 \times 10^3 + 9.5583 \times 10^7 z^2. \tag{3}$$

Differentiating Eq. (2) yields the stiffness for the second beam

$$k_b = 1.0503 \times 10^3 + 9.4614 \times 10^6 z^2. \tag{4}$$

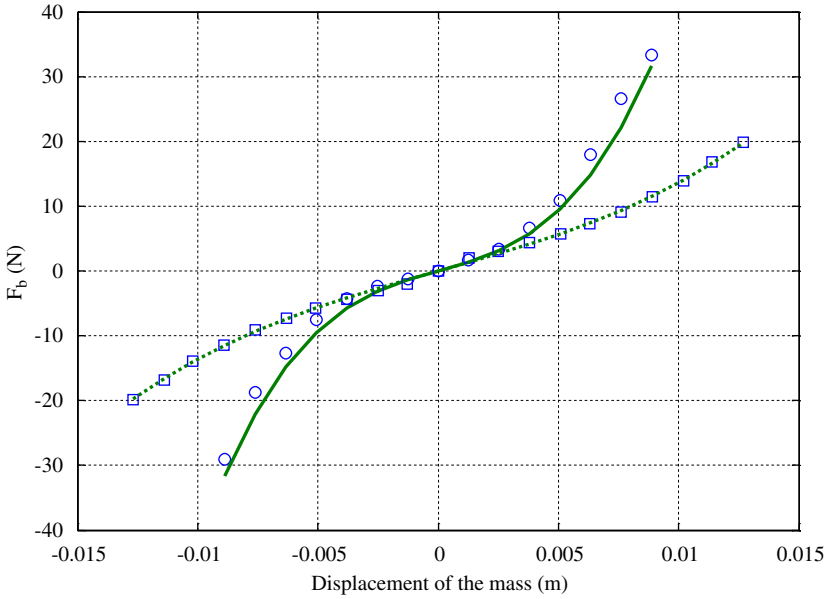

Fig. 3. The restoring force of the beam: the measured values (circles) and the best-fit curve (solid line) for the first beam; the measured values (boxes) and the best-fit curve (dotted line) for the second beam.

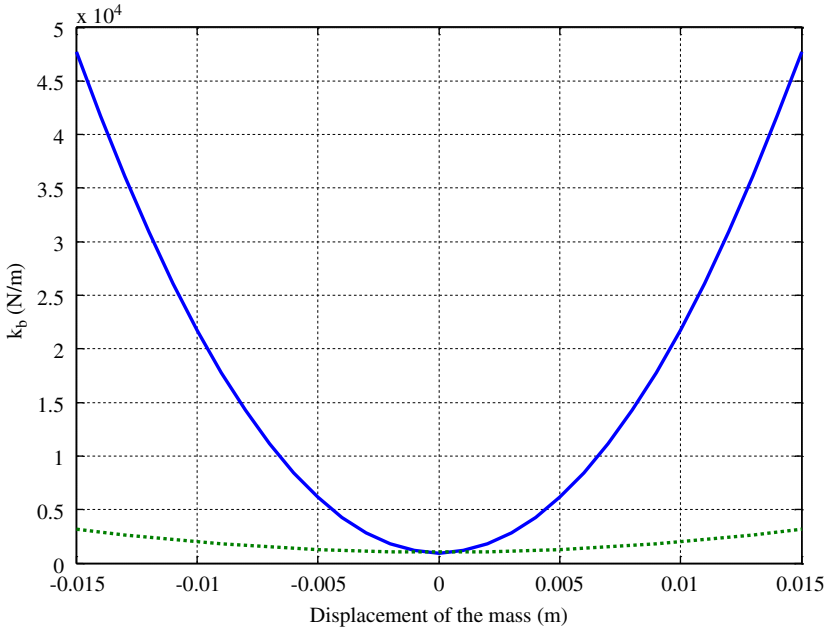

Fig. 4. Stiffness of the mechanical springs: the first beam (solid line) and the second beam (dotted line).

Fig. 4 shows the stiffness vs. the displacement of the mass for both of the mechanical springs. It is noted that the nonlinearity of the first beam is much stronger than that of the second beam. Hereinafter, the first beam is referred to as the mechanical spring with strong nonlinearity while the second beam is referred to as the mechanical spring with weak nonlinearity.

3.2. *The permanent magnet spring*

When the mass is placed between the EMs that are not energized, the interaction between the mass and the steel cores constitutes a permanent magnet spring. The mass block is formed by two neodymium magnets enclosed in an aluminum casing. The block dimension is $l \times w \times h = 25.4 \times 25.4 \times 29.0$ mm. Its magnetization is 786.23 kA m^{-1}. The analytical relationship for the attracting force between a permanent magnet block and a ferromagnetic cylinder can be found in

references such as [30]. However, some key parameters in the analytical relationship still need to be determined experimentally. Plus, it is desired to express this relationship as an explicit function of the distance between the permanent magnet and the core. Therefore, in this study, an experimental approach was taken. Using a force gauge and a dial gauge, force values between the mass and the un-energized EM were measured for different gap distances. The dots in Fig. 5 show the average results of five measurements. Coulomb's law states that the attracting or repelling force between two magnets is inversely proportional to the square of the distance between them [9]. Inspired by Coulomb's law, an analytical model for F_{pc} is assumed to be of the form

$$F_{pc} = \frac{a_1}{(d+a_2)^4}, \tag{5}$$

where d is the distance between the mass and the steel core, and a_1 and a_2 are constants to be determined. A nonlinear optimization was carried out to find the best values for a_1 and a_2 such that the sum of the squared errors between the measured values and the values computed by Eq. (5) is minimized. The solid line in Fig. 5 shows the best-fit curve obtained with the optimum values of $a_1^* = 7.7114 \times 10^{-6}\,\mathrm{N\,m^4}$ and $a_2^* = 1.6919 \times 10^{-2}\,\mathrm{m}$.

Now consider the case in which the mass is placed between the two steel cores as shown in Fig. 2. If the mass moves to the right by a distance z, the attracting force between the mass and the right core becomes

$$F_{pc1} = \frac{a_1}{(d_1+a_2)^4}, \tag{6}$$

where

$$d_1 = \frac{D-h}{2} - z, \tag{7}$$

and the attracting force between the mass and the left core becomes

$$F_{pc2} = \frac{a_1}{(d_2+a_2)^4}, \tag{8}$$

where

$$d_2 = \frac{D-h}{2} + z. \tag{9}$$

The net force acting on the mass is given as

$$\Delta F_{pc} = F_{pc2} - F_{pc1} = \frac{a_1}{(q_1+z)^4} - \frac{a_1}{(q_1-z)^4} = -8a_1q_1\frac{z(q_1^2+z^2)}{(q_1^2-z^2)^4}, \tag{10}$$

where $q_1 = (D-h)/2 + a_2$. Fig. 6 compares the experimental results and the results computed by Eq. (10) for a gap distance of $D = 70$ mm. Good agreement between the experimental results and the analytical results is obtained. The stiffness of the

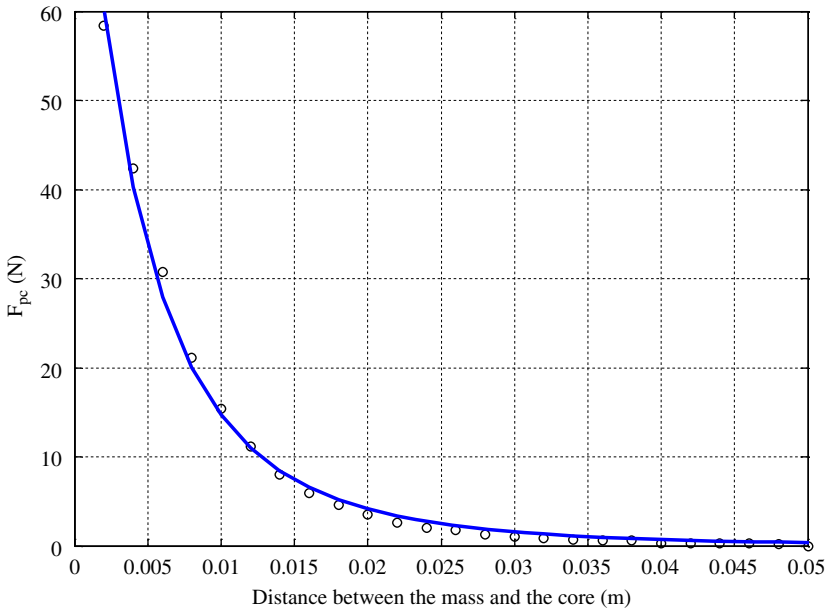

Fig. 5. Interacting force between the mass and the core; measured values (dots); and the best-fit curve (solid line).

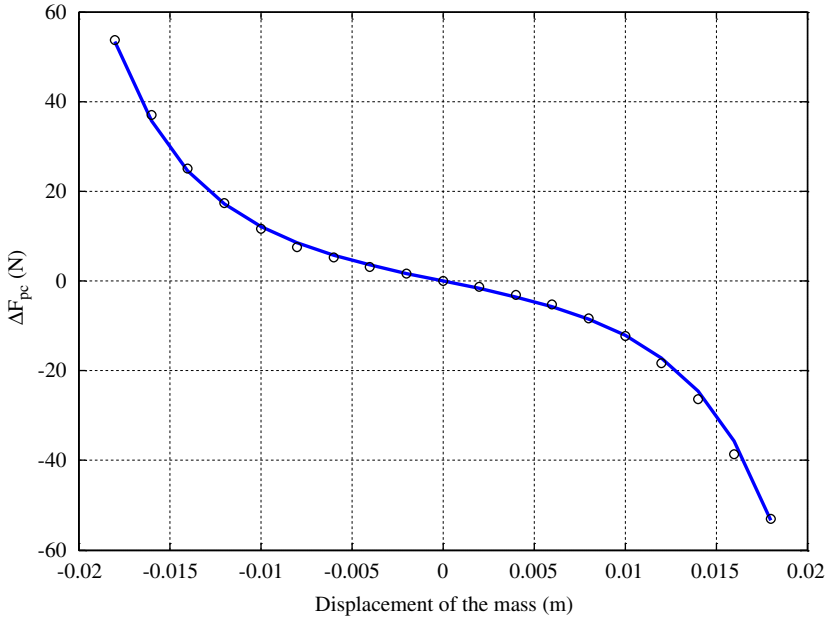

Fig. 6. Net force acting on the mass between the two steel cores with D=70 mm: the measured values (dots) and the values computed by Eq. (10) (solid line).

permanent magnetic spring can be obtained by differentiating Eq. (10) with respect to z

$$k_{\mathrm{pc}} = -8a_1q_1\frac{5z^4+10q_1^2z^2+q_1^4}{(q_1^2-z^2)^5}. \tag{11}$$

3.3. The electromagnetic spring

When the mass is placed between a pair of the EMs, the force acting on the mass depends on several factors such as the flux density produced by the EMs, the magnetization and position of the mass, and the material and size of the steel cores. To determine this force, first, consider the force due to interaction of the mass and the magnetic flux generated by one EM. According to the magnetism theory [31], the axial force acting on a permanent magnet block due to the axial magnetic flux generated by a coil can be computed by

$$F_{\mathrm{pf}} = M\left(\int_{S_1} B_d\,\mathrm{d}S - \int_{S_2} B_{d+h}\,\mathrm{d}S\right), \tag{12}$$

where M is the magnetization of the permanent magnet, S_1 and S_2 are the area of the right side and left side of the permanent magnet block, respectively (see Fig. 2), B_d and B_{d+h} are the flux density generated by the EM at S_1 and S_2, respectively. Although an analytical method to compute the axial flux density from a coil is available, some key parameters such as the magnetization of the permanent magnet and the permeability of the core still have to be determined experimentally [28].

In this study, the flux density produced by the EM was determined experimentally. To this end, the axial position away from the EM end face was divided in a step of 5.0 mm. The radial position from the axis of the EM was divided in a step of 2.5 mm. A current was applied to the EM. The flux density at each axial position and radial position was measured using a DC magnetometer (DCM, AlphaLab Inc). The results are shown in Fig. 7. It is noted that contrary to the analytical prediction [31], the flux density does not peak along the center line. Equation (12) can be approximated as

$$F_{\mathrm{pf}} = M\sum_{i=1}^{N}(B_d^i - B_{d+h}^i)\nabla S_i, \tag{13}$$

where B_d^i is the measured flux density at the axial distance d away from the EM and the radial distance r_i away from the center line of the EM, B_{d+h}^i is the measured flux density at the axial distance $d+h$ away from the EM and the radial distance r_i away from the center line of the EM, $\nabla S_i = \pi(r_{i+1}^2 - r_i^2)$ and $r_{i+1} - r_i$=2.5 mm. To simplify the computation, the square-shaped face of the permanent magnet block is approximated as a circular one with a diameter of 28.67 mm. The dots in Fig. 8 represent the results computed by Eq. (13). It can be seen that an increase in the current results in an increase of the force magnitude and an increase in the distance causes a rapid decrease in the force magnitude. A reasonable analytical

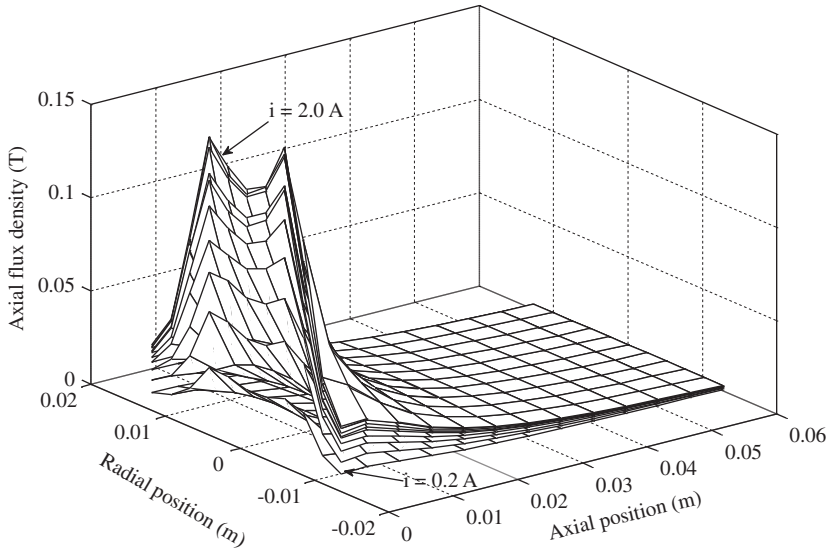

Fig. 7. Measured axial magnetic flux density of the EM for the coil currents varying from 0.2 to 2.0 A in a step of 0.2 A.

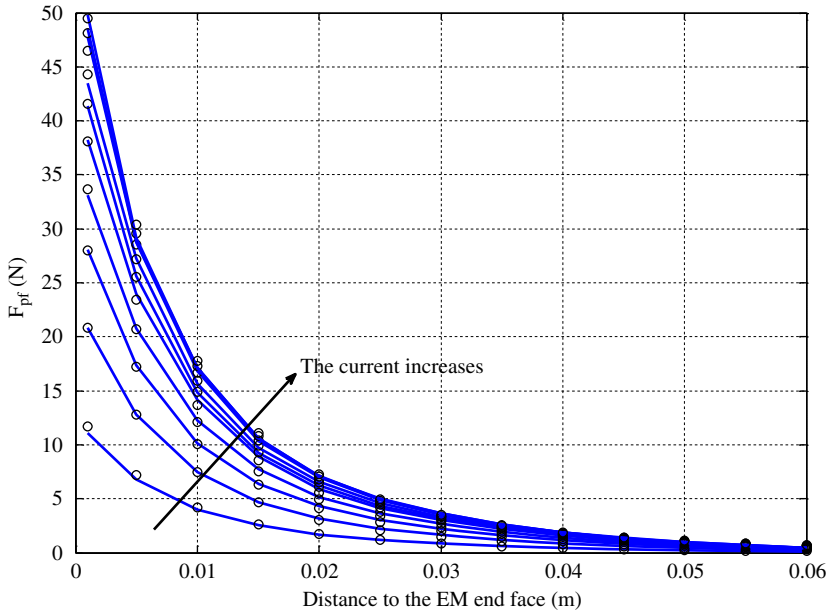

Fig. 8. Interacting force between the permanent magnet and the flux generated by the EM coil for the current varying from 0.2 to 2.0 A in a step of 0.2 A: values computed by Eq. (13) (circles) and values computed by Eq. (14) (solid line).

model may assume the following form:

$$F_{\mathrm{pf}} = \mathrm{sign}(i)(1 - \mathrm{e}^{-b_3|i|})\frac{b_1}{(d+b_2)^4}, \tag{14}$$

where $\mathrm{sign}(i) = 1$ if $i>0$, $\mathrm{sign}(i) = -1$ if $i < 0$, b_1, b_2, and b_3 are constants to be determined. A nonlinear optimization was conducted to find the optimum values for b_1, b_2, and b_3 such that the sum of the squared errors between the values computed by Eq. (13) and the values computed by Eq. (14) is minimized. The solid lines in Fig. 8 are computed using Eq. (14) with the optimum values of $b_1{}^* = 4.9192 \times 10^{-5}\,\mathrm{N\,m^4}$, $b_2{}^* = 2.9855 \times 10^{-2}\,\mathrm{m}$, and $b_3{}^* = 1.2109\,\mathrm{A^{-1}}$. It can be seen that Eq. (14) fits the varying trend of Eq. (13) well. Equation (14) will be used in the following discussion.

Next the interacting force between the mass and the EM is considered. It is tempting to obtain this force by simply adding Eqs. (5) and (14). However, many studies have shown that the relative permeability of ferromagnetic materials is sensitive to several factors such as temperature and magnetization [32,33]. For example, when an electromagnet is

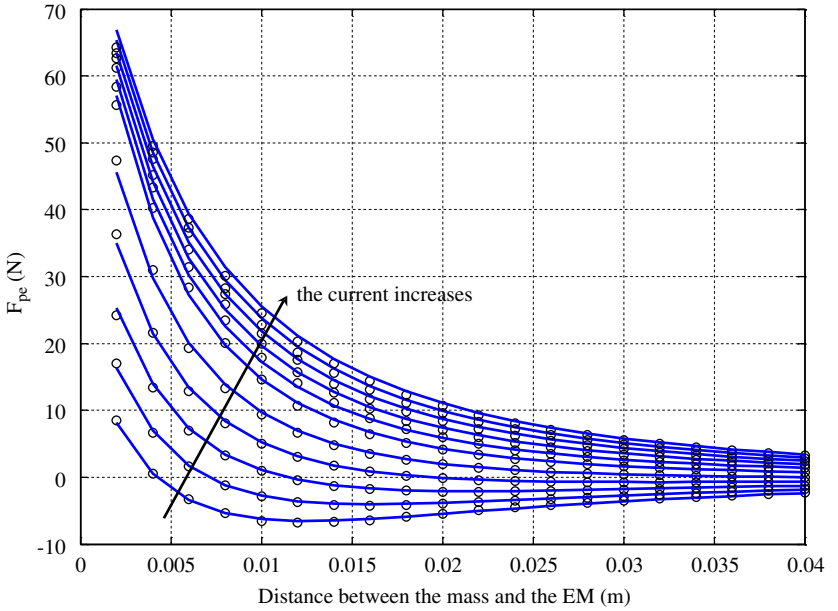

Fig. 9. Interacting forces between the mass and the EM for the currents varying from −2.0 to 2.0 A in a step of 0.4 A: measured values (circles) and values computed by Eq. (14) (solid line).

energized, the temperature of its core will rise, which inevitably alters the relative permeability of the core. And when a permanent magnet is near a ferromagnetic material, the magnetization will lower the relative permeability of the material. Considering the aforementioned reasons, an experiment was conducted to determine the interacting force between the mass and the EM. For each gap distance, the currents to the EM were varied from −2.0 to 2.0 A in a step of 0.2 A and the corresponding forces were measured. The circles in Fig. 9 show the results of five measurements. Let F_{pe} denote the force between the mass and the energized EM. This force is caused by the two aforementioned interactions, i.e.:

$$F_{pe} = e^{-a_3|i|}F_{pc} + \text{sign}(i)(1 - e^{-b_3|i|})\frac{b_1}{(d+b_2)^4}, \tag{15}$$

where F_{pc} is defined by Eq. (5) and, a_3, b_1, b_2, and b_3 are constants to be determined. The rationale of using a decaying exponential function to modify F_{pc} is based the fact that an increase in the current magnitude will reduce the relative permeability of the EM core. The b_1, b_2, and b_3 constants need to be re-determined in order to reflect the influence of the PM on the flux density. A nonlinear minimization problem was solved to determine the constants that best-fit the measured force values in the least-squares sense. The best estimated constants were found to be a_3^*=0.19343 A^{-1}, b_1^*=2.4922 × 10^{-4} N m^4, b_2^*=4.5686 × 10^{-2} m, and b_3^*=0.45038 A^{-1}. The solid lines in Fig. 9 represent the values computed by Eq. (15) with the optimum constants. It can be seen that Eq. (15) is capable of predicting the varying trends of the measured values.

When the mass placed between the two EMs displaces a distance z as shown in Fig. 2, the net force acting on the mass is given by

$$\Delta F_{pe} = F_{pe}(d_2, i) - F_{pe}(d_1, i) = -8e^{-a_3|i|}a_1q_1\frac{z(q_1^2+z^2)}{(q_1^2-z^2)^4} - 8\,\text{sign}(i)(1 - e^{-b_3|i|})b_1q_2\frac{z(q_2^2+z^2)}{(q_2^2-z^2)^4}, \tag{16}$$

where d_1 and d_2 are defined by Eqs. (7) and (9), respectively, and $q_2 = (D - h)/2 + b_2$. Differentiating Eq. (16) with respect to z yields the stiffness of the EM spring

$$k_{pe} = -8e^{-a_3|i|}a_1q_1\frac{5z^4+10q_1^2z^2+q_1^4}{(q_1^2-z^2)^5} - 8\,\text{sign}(i)(1 - e^{-b_3|i|})b_1q_2\frac{5z^4+10q_2^2z^2+q_2^4}{(q_2^2-z^2)^5}. \tag{17}$$

The above model indicates that the EM spring has two design parameters, namely the gap distance D and the current i. In the following, it is shown that D can act as an off-line tuning parameter and i as an on-line tuning parameter.

3.4. The passive HSLDS isolator

When the mass-beam assembly is placed between the electromagnets that are not energized, a passive HSLDS isolator is obtained. The stiffness of the isolator is given by

$$k = k_b + k_{pc}, \tag{18}$$

where k_b is defined by Eq. (3) or Eq. (4) and k_{pc} is defined by Eq. (11). With Eq. (3) and a prescribed D for k_{pc}, Eq. (18) gives the dynamic stiffness for the isolator with the strong nonlinear mechanical spring. Fig. 10 shows the stiffness values corresponding to four different gap distances. Compared with the solid line in Fig. 4, the PM spring softens the combined stiffness. However, the overall trend of the stiffness is still hardening. When the gap distance is too small, the stiffness around the equilibrium position becomes negative.

With Eq. (4) and a prescribed D for k_{pc}, Eq. (18) defines the dynamic stiffness for the isolator with the weak nonlinear mechanical spring. Fig. 11 shows the stiffness values corresponding to four different gap distances. In this case, the PM spring has a significant effect on the combined stiffness. When the gap distance is too small, the stiffness becomes negative. It is interesting to note that when the gap distance increases, the stiffness curve varies from a concave shape to a

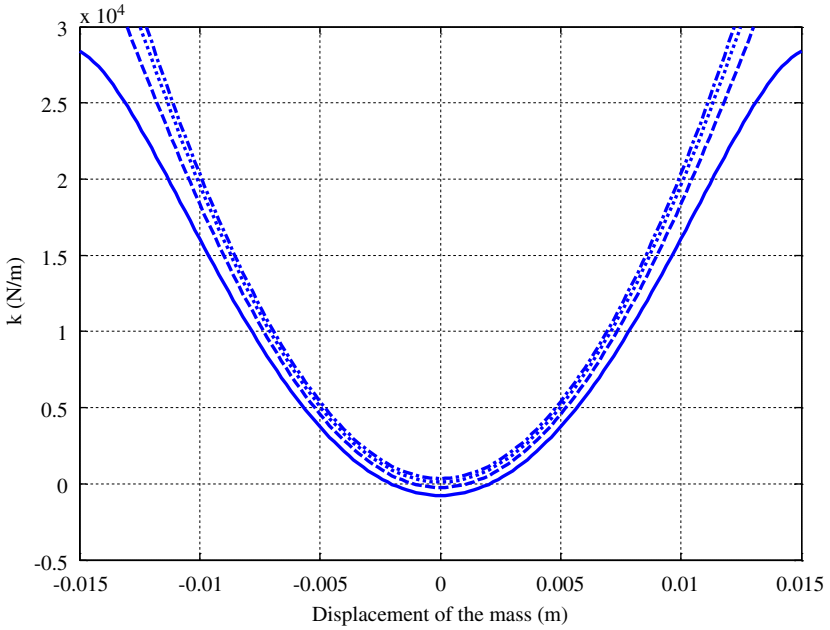

Fig. 10. Stiffness of the isolator with the strong nonlinear mechanical spring: D=60 mm (solid line); D=65 mm (dashed line); D=70 mm (dotted line); and D=75 mm (dash-dotted line).

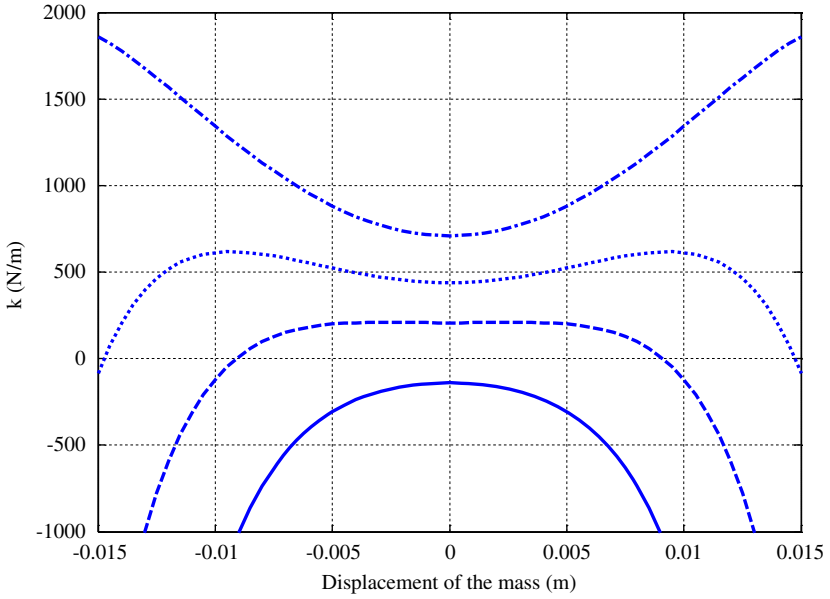

Fig. 11. Stiffness of the isolator with the weak nonlinear mechanical spring: D=65 mm (solid line); D=70 mm (dashed line); D=75 mm (dotted line); and D=85 mm (dash-dotted line).

convex one. This indicates that there exists an optimum gap distance such that the curve fluctuation around the equilibrium position can be made as small as possible. A desired region $\Delta z_{\max}$ can be defined as the maximum displacement range in which the stiffness satisfies the following condition:

$$|k - k_0| \le \varepsilon k_0 \quad \text{and} \quad k > 0, \tag{19}$$

where k_0>0 is the stiffness at the equilibrium position and ε is a prescribed tolerance. If $k < 0$, $\Delta z_{\max}$=0. Fig. 12 shows the widths of the desired region for four different tolerances. The gap distance corresponding to the peak value is the optimum gap distance that maximizes the desired region for the given tolerance. Fig. 13 shows the stiffness values of the isolators with the optimum gap distances. It can be seen that the smaller the tolerance, the smaller the stiffness variation.

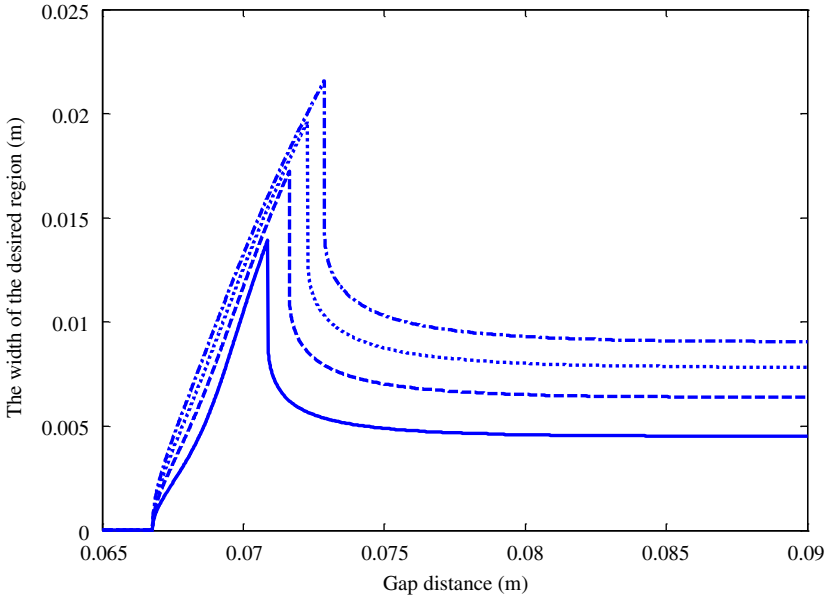

Fig. 12. The width of the desired region for the isolator with the weak nonlinear mechanical spring: ε=0.05 (solid line); ε=0.10 (dashed line); ε=0.15 (dotted line); and ε=0.20 (dash-dotted line).

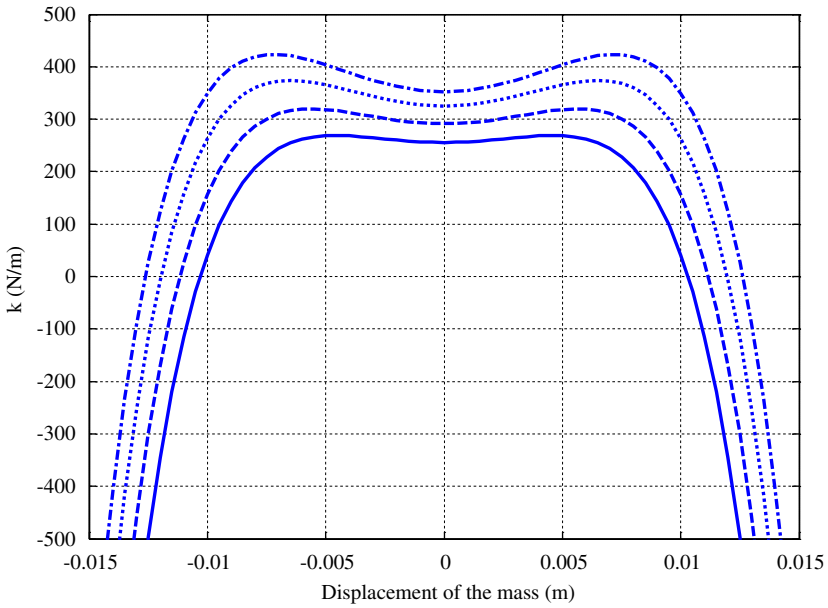

Fig. 13. Stiffness of the isolator with the optimum gap distance: D=70.87 mm (solid line); D=71.63 mm (dashed line); D=72.28 mm (dotted line); and D=72.87 mm (dash-dotted line).

Other design possibilities exist. For example, consider a nonlinear mechanical spring as given by

$$k_b = k_{b0} + k_{b1} z^2, \tag{20}$$

where k_{b0} is given and k_{b1} is to be determined. If a desired stiffness at $z=0$ is prescribed to be k_0^d, then the required gap distance can be found to be

$$D = 2\sqrt[5]{\frac{8a_1}{k_{b0} - k_0^d}} - 2a_2 + h. \tag{21}$$

If the stiffness at z_1 is desired to be k_0^d as well, then k_{b1} is given by

$$k_{b1} = \frac{k_{b0} - k_0^d - 8q_1 \dfrac{5z_1^4 + 10q_1^2 z_1^2 + q_1^4}{(q_1^2 - z_1^2)^5}}{z_1^2}. \tag{22}$$

Assume that a QZS isolator is to be designed such that $k_0^d = 0$. If the static stiffness of the mechanical spring is $k_{b0} = 1.0503 \times 10^3$ N/m, the required gap distance from Eq. (21) becomes $D = 66.75$ mm. Fig. 14 shows three stiffness curves with the k_{b1} values that are determined by specifying $z_1 = 5$, 10, and 15 mm, respectively. It can be seen that a smaller k_{b1} value will make the stiffness closer to the QZS state and the larger k_{b1} value will make the stability region wider.

3.5. The tunable HSLDS isolator

When the electromagnets are energized and the mass-beam assembly is placed between them, the stiffness of the combined system becomes

$$k = k_b + k_{\mathrm{pe}}, \tag{23}$$

where k_b is defined by Eq. (3) or (4) and k_{pe} is defined by Eq. (17). Such a set-up provides several design choices. In addition to the possibilities discussed in the previous section, the current to the electromagnets offers an on-line tuning capability. This will be explored in the experimental study. This section examines the current effect on the total stiffness. Fig. 15 shows the stiffness of the isolator with the strong nonlinear mechanical spring for four different settings. With a smaller gap distance, the softening effect of the EM spring is more noticeable. As was true in the passive HSLDS isolator, adding the EM spring to the system does not alter the hardening trend dominated by the mechanical spring. Shown in Fig. 16, the tunable isolator with the weak nonlinear mechanical spring offers more interesting variations in the dynamic stiffness. This isolator is used to investigate how the gap distance and current affect the width of the desired region defined previously. Fig. 17 shows the relationship of $\Delta z_{\max}$ vs. D and i if $\varepsilon = 0.1$.

Several observations can be drawn. When the gap distance is small, an increase of the current will cause a negative stiffness such that $\Delta z_{\max} = 0$. When the gap distance is large, the width of the desired region decreases with an increase of

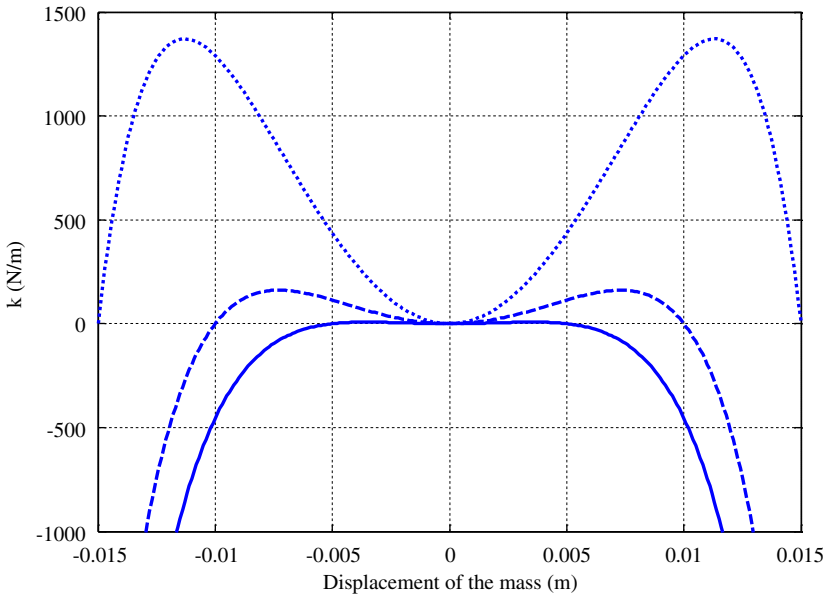

Fig. 14. Stiffness of the isolator with the optimum gap distance: $z_1 = 5$ mm, $k_{b1} = 1.34426 \times 10^7$ N/m^3 (solid line); $z_1 = 10$ mm, $k_{b1} = 1.7991 \times 10^7$ N/m^3 (dashed line); and $z_1 = 15$ mm, $k_{b1} = 3.0892 \times 10^7$ N/m^3 (dotted line).

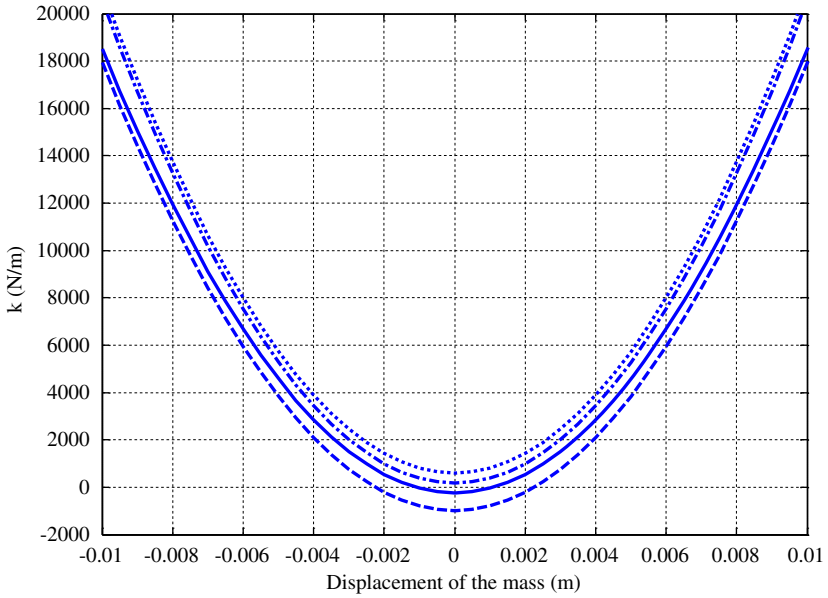

Fig. 15. Stiffness of the isolator with the strong nonlinear beam: D=65 mm and i=0 A (solid line); D=65 mm and i=2 A (dashed line); D=85 mm and i=0 A (dotted line); D=85 mm and i=2 A (dash-dotted line).

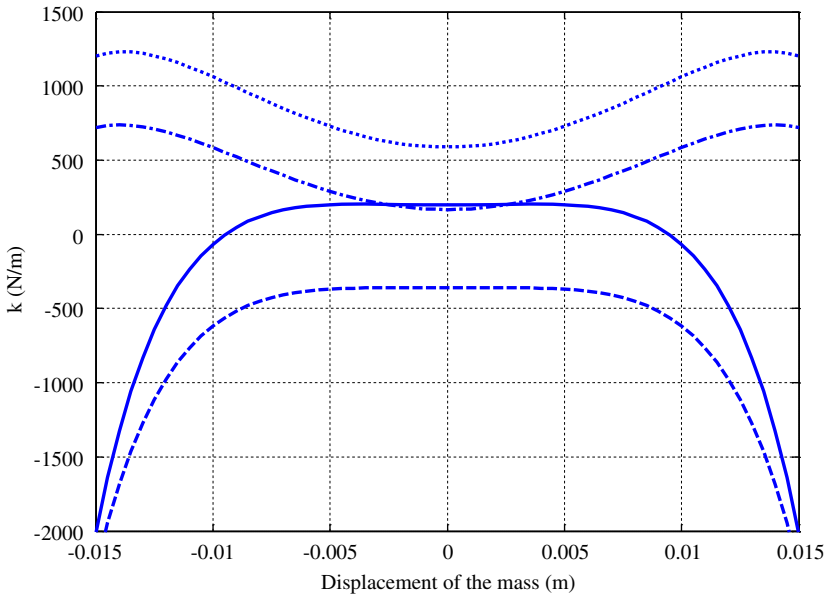

Fig. 16. Stiffness of the isolator with the weak nonlinear beam: D=70 mm and i=0.0 A (solid line); D=70 mm and i=1.5 A (dashed line); D=80 mm and i=0.0 A (dotted line); and D=80 mm and i=1.5 A (dash-dotted line).

the current. This is due to the fact that the larger the current, the smaller the stiffness at z=0 and, the more drastic the change in the stiffness curve. The Δz_{max} values peak around D=70 mm. Fig. 18 shows four stiffness curves corresponding to the optimum gap distances and the currents. It can be seen that by properly choosing the gap distance and the current, the isolator stiffness can be made nearly constant in a large range.

4. Experimental studies

A laboratory scale apparatus was built in house. Fig. 19 shows a photo of the experimental setup. The apparatus was firmly fastened to a shaking table that consists of a precision rail (6709K12) and two linear guide carts (SR20TB). The apparatus base was excited by a shaker (Brüel & Kjær, 4809) through a stinger. A PC computer with a data acquisition

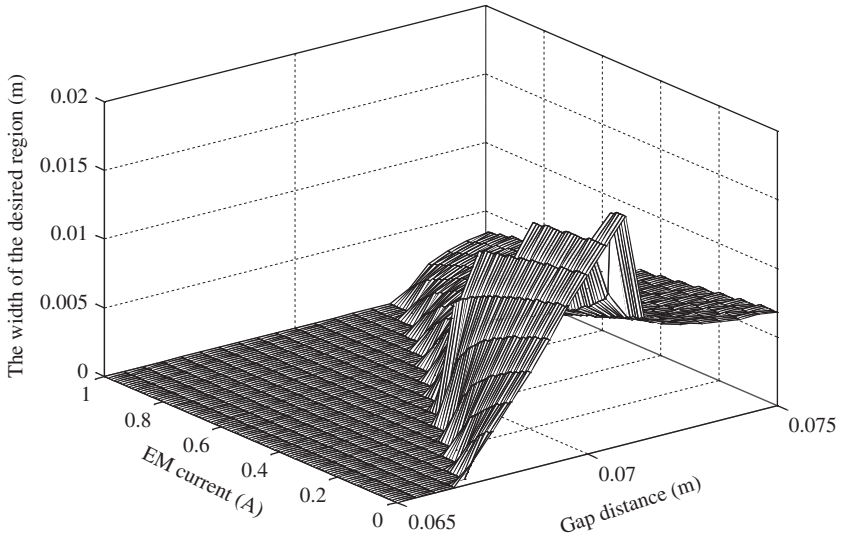

Fig. 17. The width of the desired region for the isolator with the weak nonlinear mechanical spring when ε=0.10.

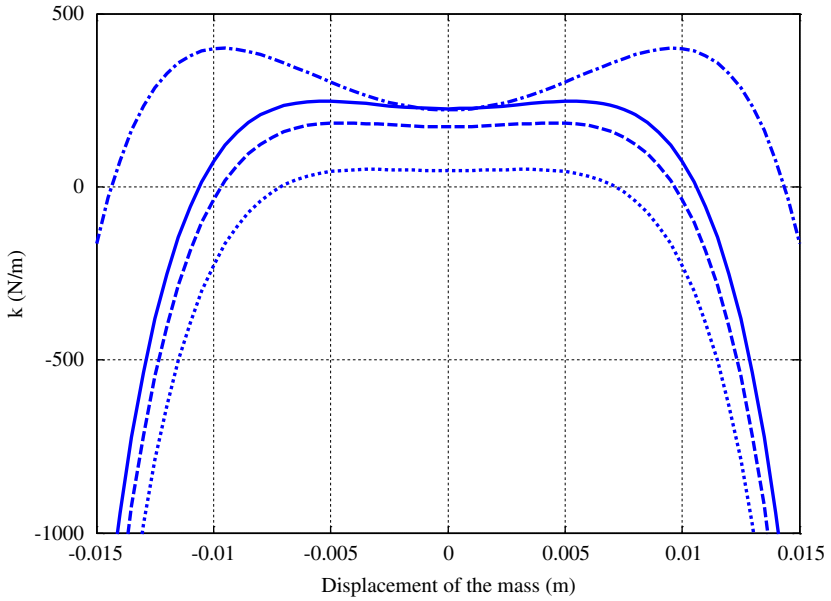

Fig. 18. Stiffness of the tunable isolator with the weak nonlinear beam: D=71 mm, i=0.05 A, and Δz_{max}=16.4 mm (solid line); D=70.5 mm, i=0.10 A, and Δz_{max}=14.4 mm (dashed line); D=70 mm, i=0.30 A, and Δz_{max}=10.6 mm (dotted line); and D=75 mm, i=0.50 A, and Δz_{max}=5.2 mm (dash-dotted line).

(DAQ) board (dSpace 1104) was used to collect response signals and generate control actions. The dSpace ControlDesk serves as the interface between Matlab, Simulink, and the DAQ board. Through one digital-to-analog channel (DAC), the generated base excitation signal was fed to a power amplifier (Brüel & Kjær, 2706) to drive the shaker. Through another DAC, the generated digital signal was fed to a linear amplifier powered by a DC power supply. The amplifier output was connected to the electromagnets with the polarity set up such that a positive/negative current created an attracting/repelling action between the PM and the EMs. A laser position sensor (Wenglor, CP24MHT80) was used to measure the displacement of the PM or the base. The signal was fed into the computer through an analog-to-digital channel (ADC). In all the tests, a sampling time of 0.001 s was used and the sampled data were processed with a numerical low-pass filter with a cut-off frequency of 60 Hz. Only the results conducted using the isolator with the strong nonlinear beam are reported below. Unless otherwise stated, the results are the average of 10 measurements.

First, the relationship between the natural frequency and the gap distance or the EM current was validated. The mass is 0.17 kg. The stiffness at the equilibrium position is computed by letting z be zero in the established models. With the mass and the stiffness, the analytical natural frequency can be determined. By tapping the mass gently, the free responses were

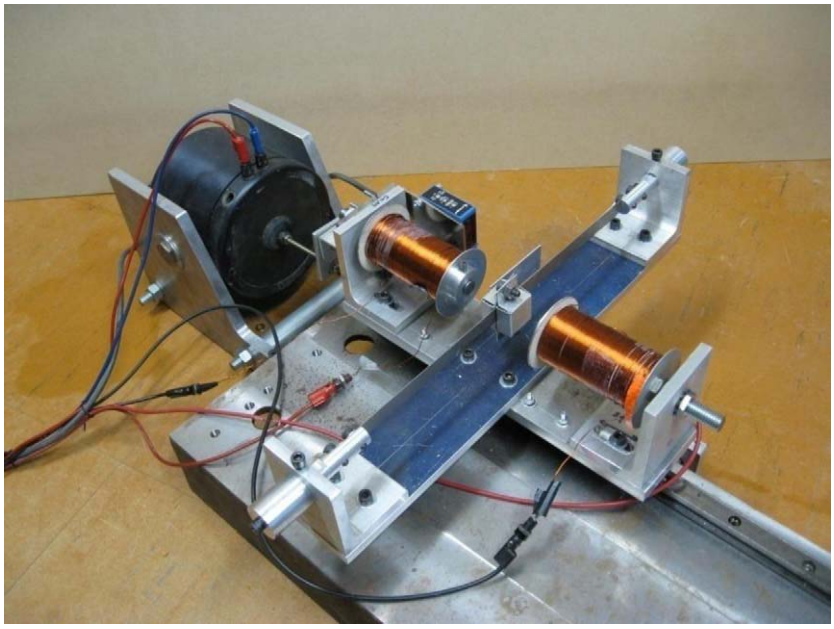

Fig. 19. Photograph of the experimental setup.

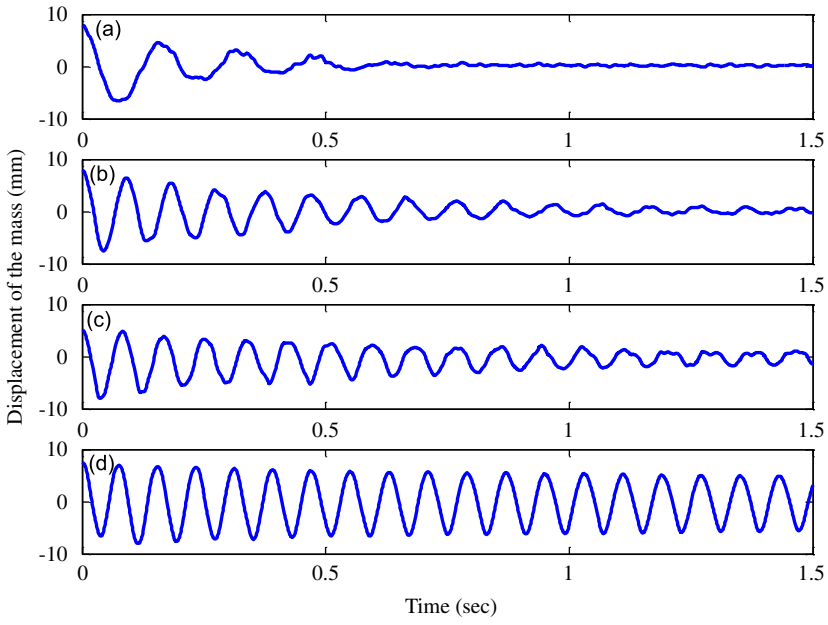

Fig. 20. Free responses of the passive vibration isolator: (a) D=70 mm; (b) D=80 mm; (c) D=90 mm; and (d) D=150 mm.

measured. Fig. 20 shows four typical responses for the passive vibration isolator. A nonlinear optimization was conducted to estimate the natural frequency ω_n and damping ratio ζ. The optimization minimizes the sum of the squared errors between the measured response and the response defined by the following:

$$z(t) = \frac{z(0)}{\sqrt{1-\zeta^2}} e^{-\zeta\omega_n t} \sin\left(\omega_n\sqrt{1-\zeta^2}t + \tan^{-1}\frac{\sqrt{1-\zeta^2}}{\zeta}\right), \tag{24}$$

which is the response of a single degree-of-freedom linear system to an initial displacement $z(0)$.

Fig. 21 shows the relationship between the natural frequency and the gap distance for the passive isolator. It can be seen that the experimental results agree well with the analytical ones. Both the results validate the trend that a decrease in

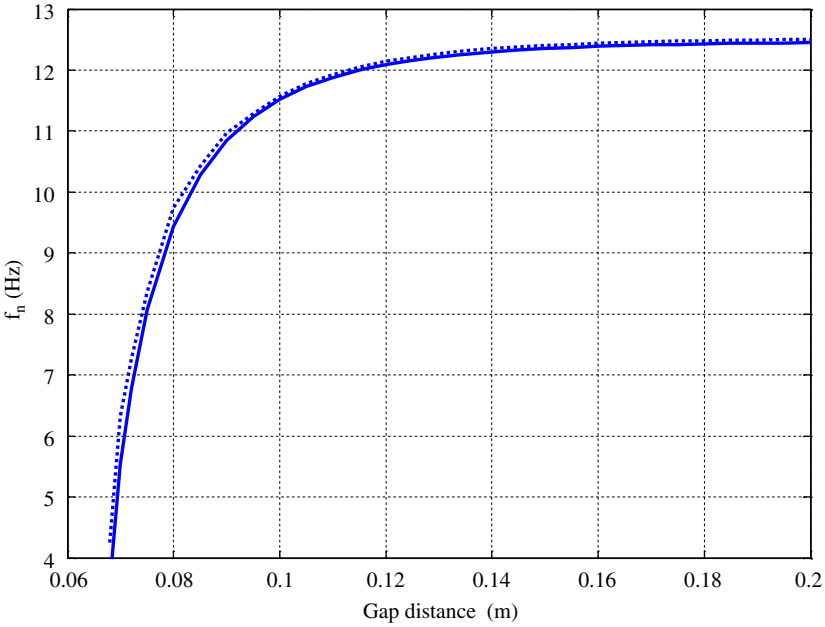

Fig. 21. Natural frequencies of the passive isolator with the strong nonlinear beam: analytical results (solid line) and experimental results (dotted line).

the gap distance lowers the natural frequency. The results also show that when the gap distance becomes large, the natural frequency becomes less sensitive to the changes in the gap distance. This is expected because the magnitude of k_{pc} is inversely proportional to D^5 as shown by Eq. (11).

The relationship between the damping ratio and the gap distance is interesting. As shown in Fig. 20, with a decrease of D, the responses decay more rapidly. With respect to Fig. 20, the estimated damping ratios are ζ=0.150 for D=70 mm, ζ=0.032 for D=80 mm, ζ=0.012 for D=90 mm, and ζ=0.005 for D=150 mm, respectively. In a linear system with a constant damping value, the damping ratio varies with the natural frequency according to the relationship: $\zeta_2 = \zeta_1\sqrt{f_{n1}/f_{n2}}$ where ζ_i is the damping ratio at the natural frequency f_{ni}. However, for the present system, the variation of the damping ratio does not follow such a relationship. This difference may be due to the effect of the eddy current and mutual induction generated by the moving permanent magnet. Fig. 22 shows the relationship between the natural frequency and the EM current for the tunable isolator with D=80 mm. Once again, both the results confirm the softening effect caused by the application of the EM currents. It is worth pointing out that the estimated values for the natural frequency and damping ratio were amplitude-dependent. A larger amplitude response tends to result in a higher natural frequency and damping ratio. This indicates that the system behaves nonlinearly.

Second, the displacement transmissibility ratio was investigated. A sinusoidal base motion with a prescribed amplitude and frequency was generated through the computer and shaker system. The steady-state response of the mass was measured. The root-mean-square (RMS) value of the 10-s response was computed. The transmissibility ratio was taken as the ratio of the RMS value of the mass displacement over that of the base displacement. By varying the exciting frequency in a step of 0.5 Hz, the relationship between the transmissibility ratio and the base exciting frequency was obtained. Fig. 23 compares the transmissibility ratios of the passive isolator for four setups when the base motion amplitude was 1 mm. With only the mechanical spring or in the absence of the PM spring, the transmissibility ratio increases with an increase of the exciting frequency up to about 18 Hz. After that, the transmissibility ratio drops drastically. A further increase of the exciting frequency makes the value of the transmissibility ratio less than one and the vibration isolation occurs. A sudden jump in the amplitude of the steady-state response is a typical phenomenon in systems with a hardening or softening nonlinearity [34,35]. In this study, the lowest exciting frequency that causes such a jump phenomenon is referred to as the jump frequency. With the PM spring, the pattern of the transmissibility ratio curve remains similar but the jump frequency shifts to the left when the gap distance decreases, which widens the vibration isolation region. It is also noted that with the PM spring, the transmissibility ratio at the low frequency region increases.

The experiment also revealed other typical behaviors of the nonlinear systems. For example, the jump frequency depends on the amplitude of the base excitation. When the exciting frequency was slightly above the jump frequency, the vibration state was very sensitive to external disturbance: an impact to the base would switch a small vibration to a large vibration. Fig. 24 demonstrates the performance of the tunable isolator with the gap distance of D=78 mm. It is observed that with an increase of the EM current, the jump frequency decreases, and therefore the isolation region is widened.

The measured transmissibility values deserve some comments. It is noted that the jump-down frequency is greater than the natural frequency computed using the stiffness at z=0. This phenomenon is expected for a system with a hardening spring [34,35]. According to [35], for a system with a cubic restoring force, the maximum transmissibility ratio $\|T\|_{max}$ is

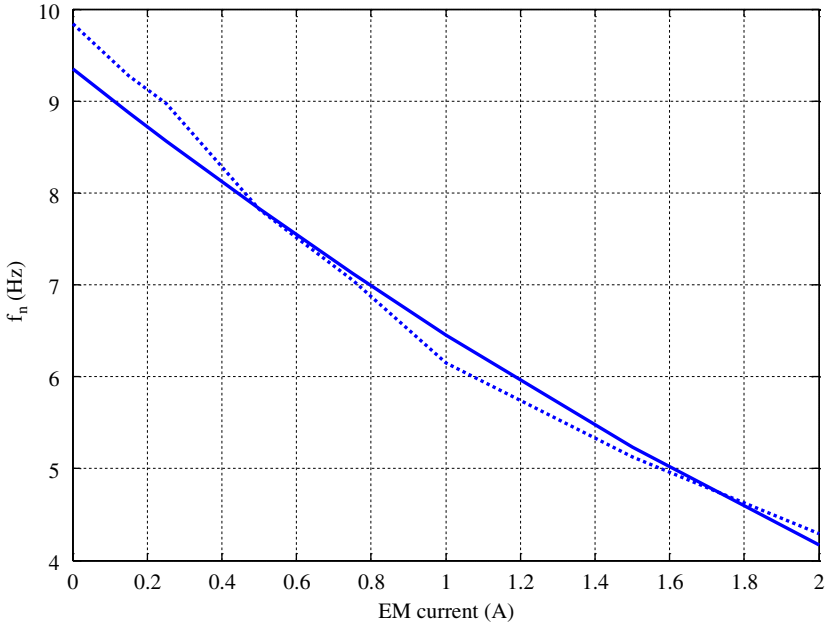

Fig. 22. Natural frequencies of the tunable isolator with the strong nonlinear beam and D=80 mm: analytical results (solid line) and experimental results (dotted line).

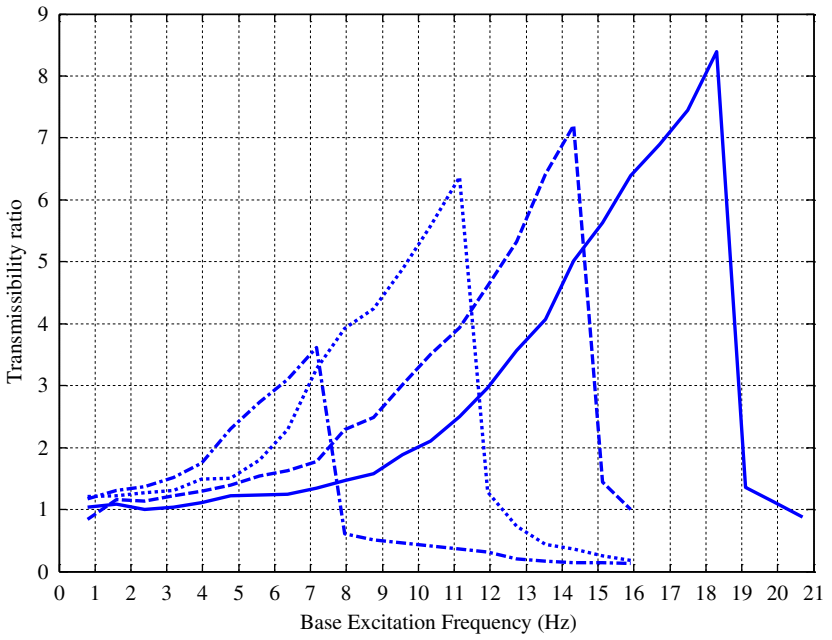

Fig. 23. Transmissibility ratios of the passive isolator for four setups: without the PM spring (solid line); D=78 mm (dashed line); D=71 mm (dotted line); and D=69 mm (dash-dotted line).

given by

$$\|T\|_{\max} = \sqrt{1 + \frac{4}{16\zeta^2 - 3\alpha}}, \tag{25}$$

where $\alpha = k_3 Z_0^2/k_1$ (see [35], for the definitions of the symbols). For a small gap distance such as D=69 or 71 mm, the maximum transmissibility ratio roughly agrees the value predicted by Eq. (25). However, for a large gap distance or without the PM spring, the measured $\|T\|_{\max}$ is smaller than the one given by Eq. (25). This result is expected, because Eq. (25) is valid only for the systems in which $\alpha < \alpha_m = 16/3\zeta^2$. For the mass-beam setup, using k_1 and k_3 given in Eq. (1), it

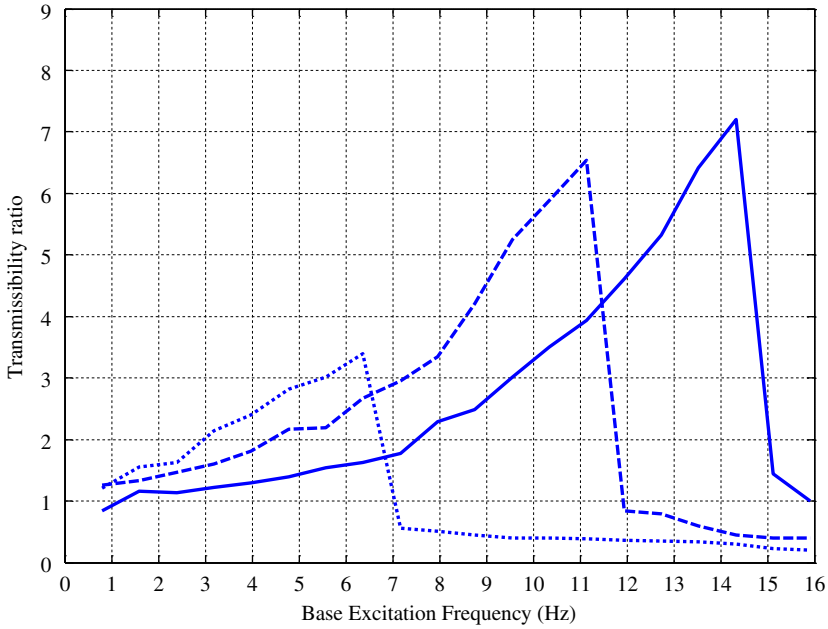

Fig. 24. Transmissibility ratios of the tunable isolator with $D=78$ mm for three setups: $i=0.0$ A (solid line); $i=1.0$ A (dashed line); and $i=2.0$ A (dotted line).

is found that $\alpha=0.030$, a value that is much greater than α_m. For the system with small damping level such as the solid line in Fig. 23, Eq. (25) is no longer valid. In this case, a numerical simulation can be used to find the transmissibility ratios. In [36], it was found that the transmissibility values determined from the numerical simulation followed the general trend of the measured values.

Third, the on-line tuning capability was explored. The objective is to achieve the best transmissibility ratio for any exciting frequency within the range of interest by adjusting the EM current. To devise a tuning strategy, refer to Fig. 24. When subjected to a given harmonic base excitation, a tunable isolator possesses two distinguishing jump frequencies. When the EM current is zero, the amplitude jump occurs at a higher frequency denoted as f_1. When the EM current is maximum, the amplitude jump occurs at a lower frequency denoted as f_2. For the isolator of Fig. 24, f_1 is about 15.0 Hz, while f_2 is about 7.0 Hz. When the exciting frequency is less than f_2, the dynamic stiffness should be as large as possible to keep the transmissibility ratio close to one. When the excitation frequency is greater than f_1, the EM current should be zero. When the exciting frequency is between f_2 and f_1, the dynamic stiffness should be reduced accordingly by varying the EM current based on the vibration magnitude.

Fig. 25 shows a Simulink model that implements such a tuning strategy. Through DAC_C8, the sinusoidal signal is sent to the shaker to generate the base motion. The displacement signal of the mass and the acceleration signal of the base are acquired through ADC_C5 and ADC_C8, respectively. Using 2048 samples, the RMS value and the main frequency of the displacement signal is computed by an embedded MATLAB function block "Cal_RMS" and by an embedded MATLAB function block "Cal_Freq", respectively. Using 2048 samples, the main frequency of the acceleration signal is computed by "Cal_Freq" as well. These two frequencies are fed into an embedded MATLAB function block "Cal_Switch" to determine which of the frequencies is more likely to be the exciting frequency. In general, the frequency determined using the acceleration signal of the base is more reliable for a high exciting frequency while the frequency determined using the displacement signal of the mass is more reliable for a low exciting frequency. The determined exciting frequency and the RMS value are sent to an embedded MATLAB function block "Cal_TuningSignal". If the RMS value exceeds a threshold value preset by the user, the following actions are taken. When the base excitation frequency is less than f_2, the EM voltage is set to a negative value so that the EM spring acts as a positive spring. When the base excitation frequency is greater than f_1, the EM voltage is zero so that the isolator becomes a passive one. When the exciting frequency is between f_2 and f_1, a positive EM voltage is determined based on the RMS value so that the dynamic stiffness is reduced. The determined EM voltage is sent to the linear amplifier through DAC_C5.

The on-line tuning strategy was tested using a base excitation of the amplitude of 0.5 mm. Fig. 26(a) compares the results of the four cases. In case one, the EM current was -1.5 A, resulting in an isolator with a high dynamic stiffness. In case two, the EM current was zero. In case three, the EM current was 1.0 A, resulting in an isolator with a low dynamic stiffness. In case four, the on-line tuning control was activated and the EM current was adjusted as shown in Fig. 25(b). It can be seen that the on-line tuning ensures that the isolator maintains the best performance.

The capability of coping with disturbance was investigated as well. Fig. 27 shows a typical result. The test was conducted using a base excitation with the frequency of 9.5 Hz and the amplitude of 0.5 mm. In the beginning, the tuning

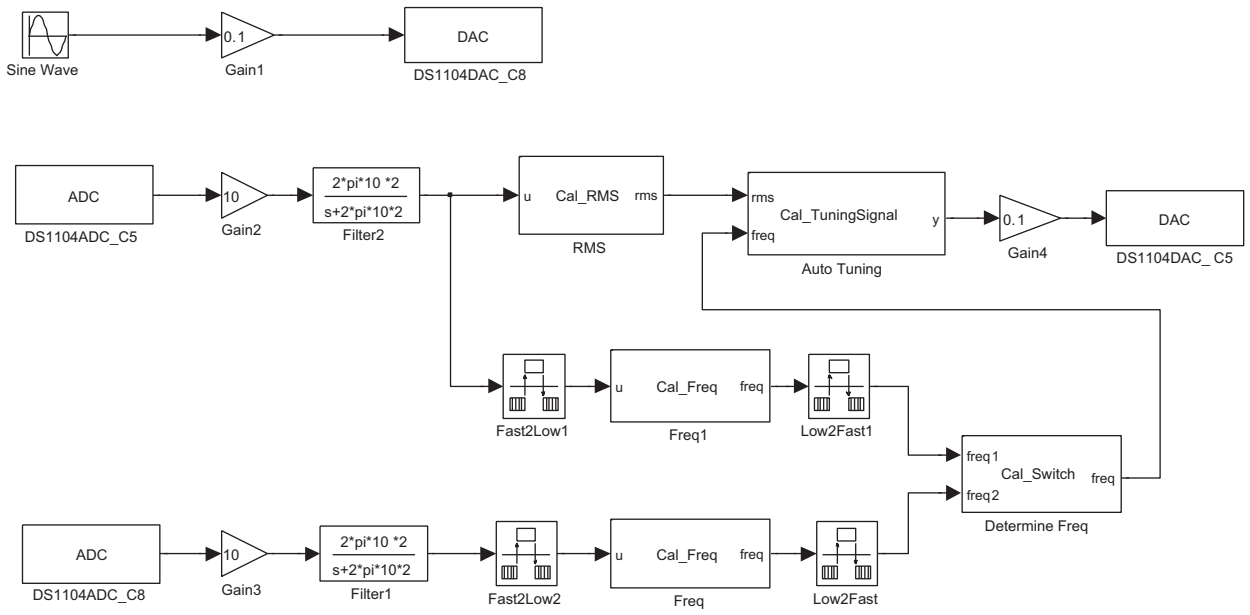

Fig. 25. Simulink model of the on-line tuning.

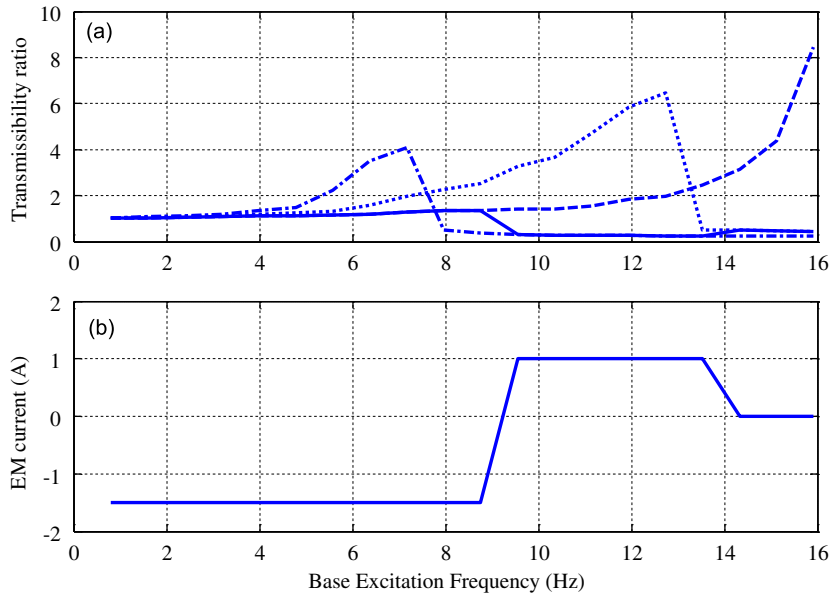

Fig. 26. (a) Transmissibility ratios of the tunable isolator for four cases: $i=-1.5$ A (dashed line); $i=0$ A (dotted line); $i=1$ A (dash-dotted line); with the online tuning (solid line) and (b) the EM current.

control set the EM current to be 1.0 A so that the smallest vibration level was established. After 3.0 s, a base disturbance was induced such that the mass jumped to a large vibration. With the tuning, the EM current was increased so that the dynamic stiffness was further reduced and the vibration was brought back to the smallest vibration level.

5. Conclusion

An electromagnetic vibration isolator, which can act passively or semi-actively, has been developed. The unique feature of the developed isolator is the tunability of its high-static–low-dynamic stiffness. A systematical approach has been devised to develop the stiffness models. The gap distance between the electromagnets has been identified as an off-line tuning parameter for the passive isolator. With the established models, the relationship between the dynamic stiffness and

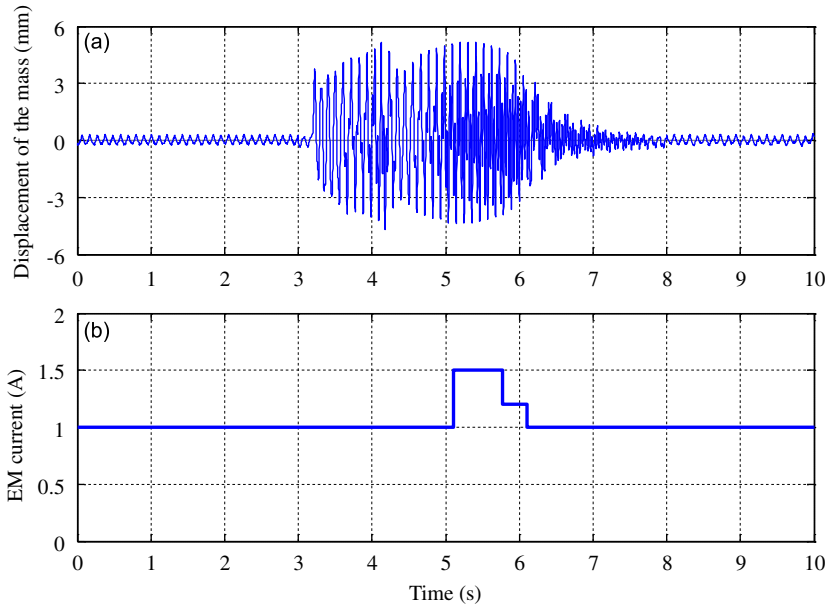

Fig. 27. (a) Response of the mass to a base excitation with the frequency of 9.5 Hz and amplitude of 0.5 mm and (b) the EM current.

the gap distance has been studied and the design optimization has been addressed. It has been shown that by properly choosing the gap distance, the isolator can possess some desired properties such as QZS or near-constant stiffness. The current to the electromagnets has been used as an on-line tuning parameter. The relationship between the dynamic stiffness and the electromagnet current has been investigated. It has been demonstrated that a proper combination of the gap distance and the electromagnet current can result in a low and near constant dynamic stiffness. A lab scale apparatus has been built. An experimental study has been conducted. The isolator's natural frequencies, determined analytically, have been validated by the measured values. The displacement transmissibility ratios of the passive isolator for different gap distances and the tunable isolator for different currents have been measured, respectively. The results have confirmed the analytical predication that reducing the gap distance or increasing the current widens the isolation region. The on-line tuning capability of the isolator has been demonstrated. The experimental results have shown that the tuning strategy can ensure the best performance when the exciting frequency varies or if the external disturbances occur.

A final note is made on the applicability of the proposed apparatus for suppression of a vertical base excitation. Although the apparatus was tested in a horizontal setup, the major results are applicable when the apparatus is used in a vertical setup in which the mass is subjected to a gravity force. It should be noted that the electromagnetic spring is independent of the gravity force. When the mass-beam assembly is installed, the mass sets down to a new equilibrium position due to a static deflection of the beam. This static deflection is very small as the stiffness of the beam is very high. Next the electromagnets are installed to ensure their symmetry with respect to the equilibrium position. As long as the mechanical spring is symmetrical about the new equilibrium position, the apparatus will work as it is used in a horizontal setup. However, it is expected that the stiffness of the beam will be somewhat asymmetric about the equilibrium position. This asymmetry makes the dynamic equilibrium position slightly different from the static one. The asymmetry problem can be minimized by taking two measures. A stiffer beam can be used to further reduce the static deflection. A higher tension can be applied to the beam to make the stiffness more linear or symmetric.

References

[1] E.I. Rivin, *Passive Vibration Isolation*, ASME Press, New York, 2003.
[2] R.A. Ibrahim, Recent advances in nonlinear passive vibration isolators, *Journal of Sound and Vibration* 314 (2008) 371–452.
[3] A. Carrella, M.J. Brennan, T.P. Waters, Static analysis of a passive vibration isolator with quasi-zero-stiffness characteristic, *Journal of Sound and Vibration* 301 (2007) 678–689.
[4] I. Kovacica, M.J. Brennan, T.P. Waters, A study of a nonlinear vibration isolator with a quasi-zero stiffness characteristic, *Journal of Sound and Vibration* 315 (2008) 700–711.
[5] D.L. Platus, Negative-stiffness-mechanism vibration isolation systems, *Proceedings of SPIE* 3786 (1999) 98–105.
[6] C.M. Lee, V.N. Goverdovskiy, A.I. Temnikov, Design of springs with "negative" stiffness to improve vehicle driver vibration isolation, *Journal of Sound and Vibration* 302 (2007) 865–874.
[7] S. Santillan, L.N. Virgin, R.H. Plaut, Equilibria and vibration of a heavy pinched loop, *Journal of Sound and Vibration* 288 (2005) 81–90.
[8] L.N. Virgin, S.T. Santillan, R.H. Plaut, Vibration isolation using extreme geometric nonlinearity, *Journal of Sound and Vibration* 315 (2008) 721–731.
[9] A. Carrella, M.J. Brennan, T.P. Waters, K. Shin, On the design of a high-static–low-dynamic stiffness isolator using linear mechanical springs and magnets, *Journal of Sound and Vibration* 315 (2008) 712–720.

[10] Y. Liu, T.P. Waters, M.J. Brennan, A comparison of semi-active damping control strategies for vibration isolation of harmonic disturbances, *Journal of Sound and Vibration* 280 (2005) 21–39.
[11] Y. Liu, T.P. Waters, M.J. Brennan, Semi-active vibration isolation system with variable stiffness and damping control, *Journal of Sound and Vibration* 313 (2008) 16–28.
[12] B. Erkus, M. Abe, Y. Fujino, Investigation of semi-active control for seismic protection of elevated highway bridges, *Engineering Structures* 24 (2002) 281–293.
[13] S. Choi, W. Kim, Vibration control of a semi-active suspension featuring electrorheological fluid dampers, *Journal of Sound and Vibration* 234 (2000) 537–546.
[14] S.B. Choi, H.K. Lee, E.G. Chang, Field test results of a semi-active ER suspension system associated with skyhook controller, *Mechatronics* 11 (2001) 345–353.
[15] Z.G. Ying, W.Q. Zhu, T.T. Soong, A stochastic optimal semi-active control strategy for ER/MR dampers, *Journal of Sound and Vibration* 259 (2003) 45–62.
[16] S. Choi, Y. Han, Vibration control of electrorheological seat suspension with human-body model using sliding mode control, *Journal of Sound and Vibration* 303 (2007) 391–404.
[17] M. Yu, X.M. Dong, S.B. Choi, C.R. Liao, Human simulated intelligent control of vehicle suspension system with MR dampers, *Journal of Sound and Vibration* 319 (2009) 753–767.
[18] M.F. Winthrop, W.P. Baker, R.G. Cobb, A variable stiffness device selection and design tool for lightly damped structures, *Journal of Sound and Vibration* 287 (2005) 667–682.
[19] J.M. Cronje, P.S. Heyns, P.W. Loveday, Development of a variable stiffness and damping tunable vibration isolator, *Journal of Vibration and Control* 11 (2005) 381–396.
[20] D. Karnopp, Permanent magnet linear motors used as variable mechanical damper for vehicle suspensions, *Vehicle System Dynamics* 18 (1989) 187–200.
[21] M. Schmid, P. Varga, Analysis of vibration-isolating systems for scanning tunneling microscopes, *Ultramicroscopy* 42–44 (1992) 1610–1615.
[22] Y. Okada, K. Matuda, H. Hashitani, Self-sensing active vibration control using the moving-coil-type actuator, *Journal of Vibration and Acoustics* 117 (1995) 411–415.
[23] Y. Matsuzaki, Y. Ishikubo, T. Kamita, T. Ikeda, Vibration control system using electromagnetic forces, *Journal of Intelligent Material Systems and Structures* 8 (1997) 751–756.
[24] K.E. Graves, D. Toncich, P.G. Iovenitti, Theoretical comparison of motional and transformer EMF device damping efficiency, *Journal of Sound Vibration* 233 (2000) 441–453.
[25] J.S. Bae, M.K. Kwak, D.J. Inman, Vibration suppression of a cantilever beam using eddy current damper, *Journal of Sound and Vibration* 284 (2005) 805–824.
[26] B. Ebrahimia, M.B. Khameseea, M.F. Golnaraghib, Design and modeling of a magnetic shock absorber based on eddy current damping effect, *Journal of Sound and Vibration* 315 (2008) 875–889.
[27] K. Liu, J. Liu, L. Liao, Application of a tunable electromagnetic damper in suppression of structural vibration, *The Transactions of the CSME* 30 (2006) 41–61.
[28] J. Liu, K. Liu, A tunable electromagnetic vibration absorber: characterization and application, *Journal of Sound and Vibration* 296 (2006) 708–724.
[29] J. Liu, K. Liu, Application of an electromagnetic vibration absorber in vibration suppression, *Structural Control and Health Monitoring* July (2008), accepted for publication.
[30] H.H. Woodson, J.R. Melcher, *Electromechanical Dynamics—Part I: Discrete Systems*, Wiley, New York, 1968.
[31] D.J. Craik, *Magnetism: Principles and Applications*, Wiley, Chichester, New York, 1995.
[32] T. Zedler, A. Nikanorov, B. Nacke, Investigation of relative magnetic permeability as input data for numerical simulation of induction surface hardening, *International Scientific Colloquium*, *Modelling for Electromagnetic Processing*, Hannover, 2008.
[33] Y. Azzouz, A. Mouillet, How to characterize soft magnetic materials by measuring magnetic flux density in a rotating field apparatus, *IEEE Transactions on Magnetics* 38 (2002) 1477–1480.
[34] M.J. Brennan, I. Kovacic, A. Carrella, T.P. Waters, On the jump-up and jump-down frequencies of the Duffing oscillator, *Journal of Sound and Vibration* 318 (2008) 1250–1261.
[35] A. Carrella, Passive Vibration Isolators with High-Static–Low-Dynamic-Stiffness, Ph.D. Thesis, ISVR, University of Southampton, 2008.
[36] N. Zhou, A Tunable High-Static–Low-Dynamic-Stiffness Isolator and Fuzzy-Neural Network Based Active Control Isolator, M.Sc. Thesis, Lakehead University, 2009.